A&A 589, A82 (2016)
DOI: 10.1051/0004-6361/201525801

Astronomy & Astrophysics

Disc colours in field and cluster spiral galaxies at $0.5 \lesssim z \lesssim 0.8$

Nicolas Cantale[1], Pascale Jablonka[1,2], Frédéric Courbin[1], Gregory Rudnick[3], Dennis Zaritsky[4], Georges Meylan[1], Vandana Desai[5], Gabriella De Lucia[6], Alfonso Aragón-Salamanca[7], Bianca M. Poggianti[8], Rose Finn[9], and Luc Simard[10]

[1] Laboratoire d'astrophysique, École Polytechnique Fédérale de Lausanne (EPFL), Observatoire de Sauverny, 1290 Versoix, Switzerland
e-mail: pascale.jablonka@epfl.ch
[2] GEPI, Observatoire de Paris, CNRS UMR 8111, Université Paris Diderot, 92125 Meudon Cedex, France
[3] University of Kansas, Dept. of Physics and Astronomy, Lawrence, 66045 Kensas, USA
[4] Steward Observatory, University of Arizona, 933 North Cherry Avenue, Tucson, AZ 85721, USA
[5] *Spitzer* Science Center, Caltech, Pasadena CA 91125, USA
[6] INAF-Astronomical Observatory of Trieste, via G.B. Tiepolo 11, 34143 Trieste, Italy
[7] School of Physics and Astronomy, University of Nottingham, University Park, Nottingham NG7 2RD, UK
[8] Osservatorio Astronomico di Padova, Vicolo dell'Osservatorio 5, 35122 Padova, Italy
[9] Department of Physics and Astronomy, Siena College, 515 Loudon Road, Loudonville, NY 12211, USA
[10] Herzberg Institute of Astrophysics, National Research Council of Canada, 5071 West Saanich Road, Victoria, BC V9E 2E7, Canada

Received 4 February 2015 / Accepted 5 January 2016

ABSTRACT

We present a detailed study of the colours of late-type galaxy discs for ten of the EDisCS galaxy clusters with $0.5 \lesssim z \lesssim 0.8$. Our cluster sample contains 172 spiral galaxies, and our control sample is composed of 96 field disc galaxies. We deconvolved their ground-based V and I images obtained with FORS2 at the VLT with initial spatial resolutions between 0.4 and 0.8 arcsec to achieve a final resolution of 0.1 arcsec with 0.05 arcsec pixels, which is close to the resolution of the ACS at the HST. After removing the central region of each galaxy to avoid pollution by the bulges, we measured the $V - I$ colours of the discs. We find that 50% of cluster spiral galaxies have disc $V - I$ colours redder by more than 1σ of the mean colours of their field counterparts. This is well above the 16% expected for a normal distribution centred on the field disc properties. The prominence of galaxies with red discs depends neither on the mass of their parent cluster nor on the distance of the galaxies to the cluster cores. Passive spiral galaxies constitute 20% of our sample. These systems are not abnormally dusty. They are are made of old stars and are located on the cluster red sequences. Another 24% of our sample is composed of galaxies that are still active and star forming, but less so than galaxies with similar morphologies in the field. These galaxies are naturally located in the blue sequence of their parent cluster colour–magnitude diagrams. The reddest of the discs in clusters must have stopped forming stars more than ~5 Gyr ago. Some of them are found among infalling galaxies, suggesting preprocessing. Our results confirm that galaxies are able to continue forming stars for some significant period of time after being accreted into clusters, and suggest that star formation can decline on seemingly long (1 to 5 Gyr) timescales.

Key words. methods: data analysis – galaxies: clusters: general – galaxies: evolution

1. Introduction

Galaxy evolution is influenced by their environment (for a review of the seminal works see Blanton & Moustakas 2009), although the exact mechanisms at play and their sphere of influence still need to be unveiled (Villalobos et al. 2012; Haines et al. 2015; Woo et al. 2015; Bahé & McCarthy 2015). There are indeed spectacular signs of perturbations induced by the infall of galaxies in clusters, such as the stripping of the neutral gas (e.g. Chung et al. 2009) and complex perturbed morphologies (e.g. Ebeling et al. 2014). Some signs are more subtle but nevertheless involve a large portion of a galaxy population, such as the decrease in star formation rate (e.g. Poggianti et al. 2008; Fumagalli & Gavazzi 2008) or the emergence of lenticular galaxies (S0) and corresponding decline in spirals (e.g. Desai et al. 2007; Just et al. 2010). Although spiral disc fading is not a sufficient explanation for the rise of S0s (Christlein & Zabludoff 2004), spirals are strongly affected both in numbers and properties by dense environments. Clues to the intensity and timescale of the processes at play are to be found in gas content and stellar population properties (e.g. Rodríguez Del Pino et al. 2014).

The link between the hot gas, which is heated by young stars, and the galaxy stellar component has essentially been investigated from the standpoint of their spatial distribution. At intermediate redshift, Bamford et al. (2007) showed that while the stellar disc scale lengths remain similar in field and cluster spirals, the extent of the emission line regions is smaller in cluster systems. Jaffé et al. (2011) found that kinematically disturbed star-forming galaxies are more frequent in clusters than in the field, but the presence of kinematically disturbed gas and morphological distortions are almost not correlated at all. They also showed evidence that the gas discs in cluster galaxies are truncated, with star formation more concentrated than in a low-density environment. These results are in line with those of Maltby et al. (2012), who found with STAGES (the Space Telescope A901/2 Galaxy Evolution Survey, Gray et al. 2009) that the galaxy environment does not affect the stellar distribution of the outer discs, but contrasts with studies in higher

Table 1. Properties of the galaxy clusters.

Cluster ID	z_{cl}	σ_{cl} [km s^{-1}]	R_{max}/R_{200}	N_{clus}	N_{field}	Sa-Sab	Sb-Sbc	Sc-Scd	Sd
cl1037.9-1243	0.5805	319^{+53}_{-52}	1.99	11	14	3	6	1	1
cl1040.7-1155	0.7043	418^{+55}_{-46}	1.84	19	24	4	7	7	1
cl1054.4-1146	0.6972	589^{+78}_{-70}	1.85	20	12	5	9	5	1
cl1054.7-1245	0.7502	504^{+113}_{-65}	1.49	13	8	7	3	3	0
cl1103.7-1245b	0.7031	252^{+65}_{-85}	2.71	6	11	0	3	3	0
cl1138.2-1133	0.4788	732^{+72}_{-76}	0.61	26	3	6	4	14	2
cl1216.8-1201	0.7955	1018^{+73}_{-77}	0.96	28	3	7	6	13	2
cl1227.9-1138	0.6357	574^{+72}_{-75}	1.36	13	12	4	7	2	0
cl1232.5-1250	0.5419	1080^{+119}_{-89}	0.71	26	3	12	12	2	0
cl1354.2-1230	0.7620	648^{+105}_{-110}	1.59	10	6	1	5	4	0

Notes. The table includes cluster name, redshift (z_{cl}), velocity dispersion (σ_{cl}), radius of the region covered by the observations in units of R_{200} (R_{max}), number of field spiral galaxies defined as non-cluster member, but whose redshift falls within $\Delta z \leq 0.1$ of z_{cl} (N_{field}), number of cluster galaxies per Hubble type.

density environments such as the Coma and Virgo clusters. In these, the stellar scale lengths of the disc galaxies were measured to be 20−30% smaller than those in the field (Aguerri et al. 2004; Gutiérrez et al. 2004; Koopmann et al. 2006).

The stellar population properties make a decomposition into bulge and disc galaxies necessary. Hudson et al. (2010) analysed eight nearby clusters ($z \leq 0.06$, $700 < \sigma < 1000$ km s^{-1}) and inferred that while the $B-R$ colours of the bulge components do not significantly depend on the environment, the discs in the cluster centre are redder than those at the virial radius and even more redder than the discs of the field spirals. This was also confirmed by Head et al. (2014) in the Coma cluster. Our work is part of a global observational effort to help identify how spirals are transformed in dense regions. Establishing where and when the stellar populations of cluster spiral discs differ from those in field analogues provides critical information on the gas-removal timescales for the bulk of the cluster galaxy population. To do this, we place our study at intermediate redshift, when both star formation and quenching are still in full swing (Rudnick et al. 2009; Finn et al. 2010)

Distinguishing bulge and disc properties at intermediate and high redshifts requires at least spatial resolutions and samplings comparable with those achieved with the HST in at least two photometric bands. This type of dataset is not always available, particularly in the case of large ground-based surveys. The deconvolution technique offers a unique alternative. It is very efficient when applied to objects with scales close to the point spread function (PSF) size and presents a number of crucial advantages. First, the absence of priors on the underlying galaxy profiles, classically imposed with analytical formulae, is expected to provide more robust results. Second, because the PSF is essentially removed, the resolution of the deconvolved images can be controlled and fixed for an entire sample despite very different original observing conditions. Third, the improved sampling, combined with the higher resolution and the PSF removal, allows studying those parts of the galaxies that were previously buried inside the PSF. The better the sampling of the initial PSF, the finer the results of the deconvolution.

In the following, we present the first analysis of spiral disc colours in a sample of intermediate-redshift cluster galaxies by applying our deconvolution technique to a set of images obtained with the FORS2 camera at the VLT. Our sample is drawn from the ESO Distant Cluster Survey (EDisCS, White et al. 2005) and allows us to investigate trends with cluster masses and lookback-time. Because the EDisCS clusters were only observed with the ACS at the HST in the *F814W* filter, our deconvolution method provides a unique opportunity of retrieving the galaxy properties at high spatial resolution from the ground-based FORS2 multi-band observations.

We present our dataset in Sect. 2. An overview of the deconvolution procedure is provided in Sect. 3. Section 4 presents our main results, which are discussed in Sect. 5 and summarized in Sect. 6.

2. EDisCS cluster sample

EDisCS is an ESO Large Programme dedicated to the analysis of 20 galaxy clusters in the redshift range $0.4 \lesssim z \lesssim 1$, spanning a wide range of masses, that is, of velocity dispersions, from ∼200 km s^{-1} to ∼1000 km s^{-1} (Halliday et al. 2004; Milvang-Jensen et al. 2008). These clusters were initially selected from the most significant brightness peaks in the Las Campanas Distant Cluster Survey (LCDCS; Gonzalez et al. 2001). They all benefit from deep B, V, R, and I photometry obtained with FORS2 at the VLT (White et al. 2005). A subset of ten clusters was also imaged with the ACS at the HST in the *F814W* filter (White et al. 2005; Desai et al. 2007); they constitute the basis of the present study.

For the purpose of our analysis, we distinguish cluster and field populations based on the cluster redshift, z_{cl}, and cluster velocity dispersion, σ_{cl}. The cluster members are the galaxies with spectroscopic redshifts within $\pm 3\sigma_{cl}$ (Halliday et al. 2004; Milvang-Jensen et al. 2008). This spectroscopic sample is magnitude limited at $I \sim 23$ mag measured in 1 arcsec radius apertures, with the exception of cl1232.5-1250, at lower redshift, for which the limit is $I = 22$ mag (Halliday et al. 2004). As discussed in Poggianti et al. (2006), we were able to build an I-band selected unbiased sample of field galaxies with the same exact observational conditions as the cluster members by selecting galaxies that are not cluster members in each observed spectroscopic mask, but have redshifts within $\delta z = \pm 0.1$ of the targeted cluster redshift.

From the original sample of 350 spectroscopically confirmed cluster members, we selected the spiral galaxies with T-type between 1 and 7, that is, with Hubble types between Sa/SBa and Sd/SBd. The final set of galaxy members comprises 172 cluster members. The full control sample encompasses 196 field galaxies, from which 96 have Sa/SBa to Sd/SBd types and redshifts

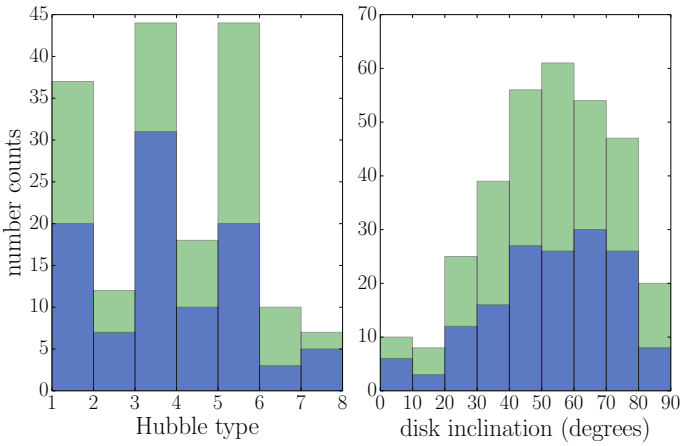

Fig. 1. Comparison of the distribution into Hubble types and inclinations between our cluster and field galaxy samples. The cluster and field galaxies are plotted in green and blue, respectively.

$0.45 \leq z_{\rm spec} < 0.81$. Table 1 summarises the number of cluster and field galaxies found in each cluster field as explained above together with their morphologies. They constitute our full sample, which is grouped into redshift bins later in the analysis.

Figure 1 displays the visually classified morphological types (Desai et al. 2007) of our sample galaxies and the distribution of the inclination angles as measured from GIM2D (Simard et al. 2009). The uncertainty on the morphological classification is of the order of one Hubble type. The cluster members and field galaxies display almost identical distributions and can thus be safely compared free of biases that might have been generated by differential dust obscuration or different morphologies.

3. Photometry

3.1. Image deconvolution

Most cluster galaxies are small at $0.5 \lesssim z \lesssim 0.8$. Spiral bulges, whose effective radii are of the order of 2−3 ACS pixels, are therefore barely resolved even with the HST. The PSF full width at half maximum (FWHM) of images obtained with FORS2 at the VLT lies between 0.48″ and 0.85″, depending on the photometric band and the observing night. The complete photometric description, with the seeings and exposure times of each cluster, is accessible in White et al. (2005). These resolutions cause the bulge light to leak onto the disc component and adjust all images to the same resolution, as is classically done in photometric measurements. which further degrades the situation and makes studying the discs impossible.

To distinguish the contribution of the different galaxy components to the total luminosity, multi-component model fitting is often carried out. The impact of the PSF is taken into account to deliver PSF-free galaxy models as well as possible (e.g. Simard et al. 2002; Peng et al. 2011; Vika et al. 2013). Nevertheless, the choice of the analytical functions is somewhat arbitrary and does not necessarily apply to all galaxies. The case of galaxies perturbed by gravitational interactions constitute a clear problem for which a general analytical solution is not trivial, if it is possible at all. Therefore, we aim at avoiding any prior on the shape of the galaxy components. The first step is to access the galaxy morphologies directly, that is, visually. This is done by converting the original FORS2 images to a common and much smaller resolution with a finer sampling similar to that of the HST. The photometric measurements are then performed on these deconvolved images. In the following the HST images are only used as a posteriori checks of the reliability of the deconvolution. They are not used as priors.

We used an improved version of the MCS image deconvolution algorithm (Magain et al. 1998), because sampled images cannot be fully deconvolved without violating the sampling theorem. Instead, the images are partially deconvolved, meaning that we aim at an improved instead of an infinite resolution. As a consequence, the PSF in the deconvolved image (“target” PSF) can be chosen in such a way that it is well sampled. In practice, the shape of the target PSF is chosen to be a circular Gaussian. The description of the new algorithm is presented in Cantale et al. (2016). The new features, which specifically benefited from the deconvolution of the EDisCS data, are an efficient regularization strategy, a new minimization, and a proper noise treatment. The new regularization uses a multi-scale approach to eliminate the high frequencies where no signal is present. Special care was also taken in the proper noise treatment. An incorrect estimate of the noise may lead to significant errors in the final photometry.

The algorithm uses super-resolved PSFs, constructed from several stars in the field of view (two to six stars, depending on the cluster), with a smaller pixel scale than in the original image. The stars were selected from the brightest stars, without neighbours and close to the cluster centre, in such as way that the PSF corresponds to the region in which the galaxies are located. We chose the pixel size to be four times smaller than the original size and a target PSF sampled with two of these pixels at FWHM. In other words, the resolution in our deconvolved images is 0.1″ with a pixel size of 0.05″, which is similar to the data from the ACS at the HST. All our images are therefore fully numerical (as opposed to described by an analytical function), and the only prior on the light distribution imposed by the regularization is a pixel-to-pixel continuity.

Figure 2 shows a few examples of deconvolution over the full redshift range of our sample. The galaxies were chosen to span a broad range of angular sizes, compactness, and number of substructures. We show the I-band images of the FORS2 at the VLT, their deconvolved counterparts, the residual maps, and the corresponding $F814W$ images obtained with the ACS at the HST. The residual maps are the difference between the original VLT image and its deconvolution, in units of photometric noise. These are displayed between -3σ (white) and $+3\sigma$ (black). The red circles correspond to the aperture applied to remove the bulge light, as explained in Sect. 3.2. The complexity of the galaxy morphologies and the small-size features such as star-forming regions, faint spiral arms, or even dust lanes are unveiled by the deconvolution procedure. They are all confirmed by the comparison with the ACS images. Most of the time, the residual maps reveal only negligible structures, which illustrates the excellent quality of our procedure. Only the regions with very peaked luminosity profiles are difficult to fit because of the regularization and yield large residuals.

3.2. Aperture photometry

We performed aperture photometry with `SExtractor` (Bertin & Arnouts 1996). The centroids and the shapes of the global apertures were drawn from the original I-band FORS2 data, taken as reference images, the photometric measurements were subsequently carried out on the V-band and I-band deconvolved frames at a resolution of 0.1″. The apertures used to compute

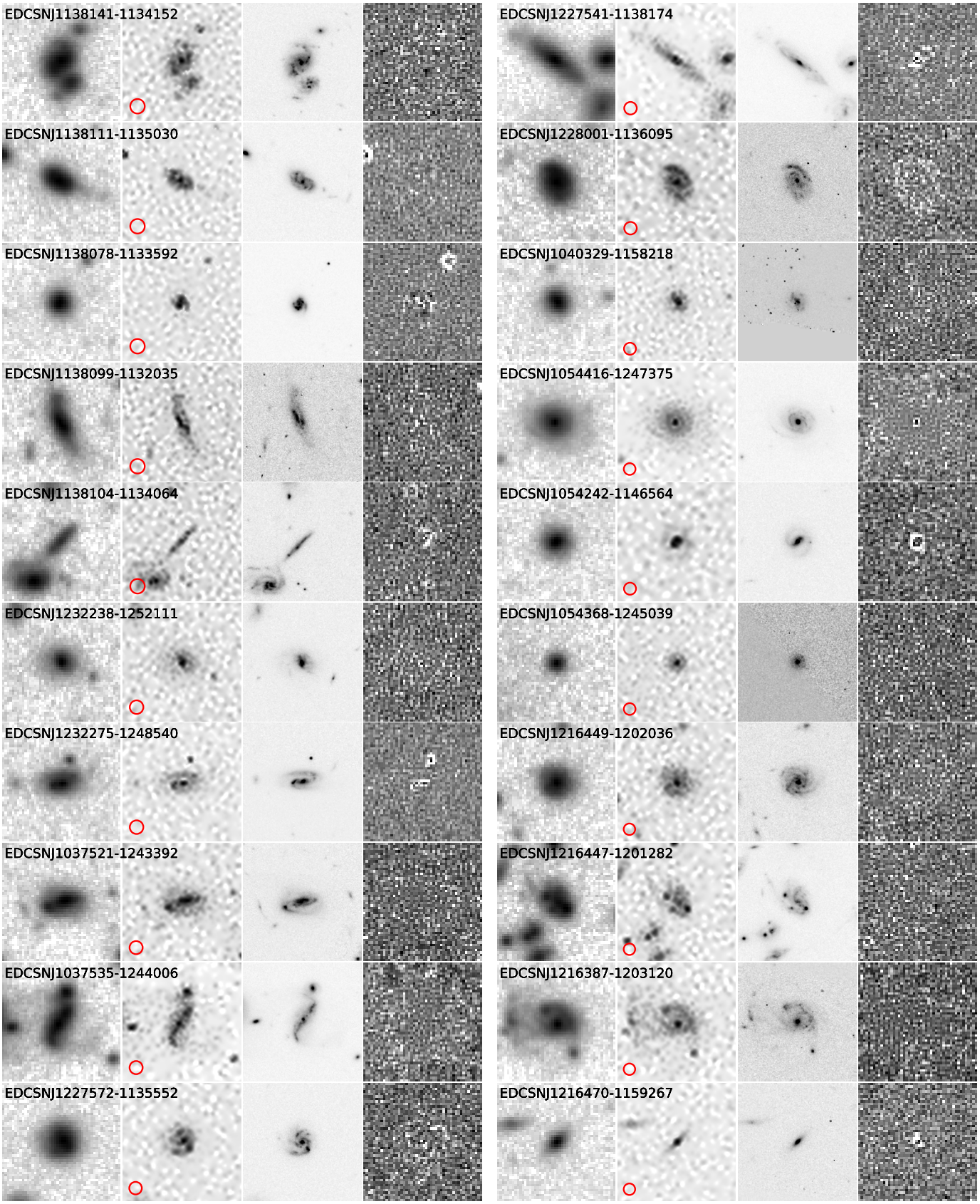

Fig. 2. Examples of deconvolving the EDisCS spiral galaxies over the whole redshift range. *From left to right*, the columns show (i) the original *I*-band images obtained with FORS2 at the VLT with seeing between 0.5″ and 0.7″; (ii) their corresponding deconvolved VLT images with a resolution of 0.1″; (iii) the images obtained with the ACS at the HST in the *F814W* filter for comparison; and (iv) the residual images in units of the photon noise between the initial FORS2 images and their deconvolution. The red circles represent the 3.5 kpc circular aperture used to remove the bulge contribution. The similarities between the VLT deconvolutions and the HST images are striking: details such as spiral arms or dust lanes previously smeared out by the PSF are made visible and are confirmed by the HST images.

the total object magnitudes are the Kron-like elliptical aperture from SExtractor.The photometric error bars are given by the photon noise in the aperture:

$$m_{\rm err} = 2.5 \cdot \log_{10}\left(1 + \frac{\sqrt{F_{\rm aper} + \sigma^2_{\rm sky}}}{F_{\rm aper}}\right), \quad (1)$$

where $F_{\rm aper}$ is the total photon number counts in the aperture, that is, the counts corresponding to the sum of the sub-exposure images and converted into electrons; $\sigma_{\rm sky}$ is the sky noise in the full image, corresponding to the standard deviation in the empty regions of the original image, as estimated on the full image. This is the same as the image used during the deconvolution.

The flux of the disc component was recovered by subtracting the bulge contribution from the galaxy total luminosity. The total galaxy flux was measured in an elliptical aperture, while the flux of the galaxy bulge was calculated in a circular aperture. The apertures were identical in V and I bands.

This method obviously requires the size of bulge aperture to be carefully chosen. It must be sufficiently small to include most of the disc component, but large enough to account for the diversity of bulges along the Hubble sequence. To fix this minimum size, we used the great variety of bulge and disc profiles of the sample of face-on nearby spirals reported in de Jong (1996) to build model galaxies with redshifts, signal-to-noise ratios, angular sizes, and resolution similar to those in our sample. By varying the aperture radii, we calculated the flux of all simulated galaxies. There is no PSF at this stage. We requested a maximum 5% error on the recovered disc fluxes, that is, a negligible pollution by the bulge. This corresponds to 0.05 mag, which is smaller than our photon noise errors (see below), and an aperture of $r = 1.5$ kpc. Then, we evaluated the impact of the PSF. Although the deconvolution brings the images to a much improved spatial resolution, there is still a PSF to be taken into account, since we deconvolve to a finite resolution. This means that the deconvolved data represent the true light distribution, convolved by the Gaussian PSF of 0.1″ FWHM. This, combined with the necessary regularization inherent to the deconvolution, which also causes spreading of the light, prevents the deconvolved data from reaching the true light distribution in the inner parts of very sharp profiles. This affects the photometry of the bulges, with a leakage of their light beyond the physical theoretical limit. The left panel of Fig. 3 presents the difference between the I-band magnitudes integrated in the images obtained with ACS at the HST and in the original FORS2 images as a function of the aperture radius, while the right panel of the same figure presents the difference between the aperture magnitudes calculated in the images of the ACS at the HST and in the final deconvolved I-band FORS2 images. As revealed by the large difference between the HST and original-FORS2 magnitudes, the bulge light leaks onto the disc from the inner regions to far out. The deconvolution does not deal easily with sharp unresolved profiles. This is a consequence of our choice not to introduce any a priori analytical profile: unresolved features, such as point sources or bulges, conflict with the regularization. Nevertheless, after deconvolution, the HST and the VLT (deconvolved) magnitudes agree on average to within ∼0.05 mag (rms) in an aperture as small as 0.3″. This corresponds to a physical aperture of 2.2 kpc, which we represent by a dotted red line for the highest redshift galaxies. We note that we cannot conclude for objects below this limit because the HST PSF itself affects the profiles: within a 0.3″ aperture, the encircled energy of the HST PSF is about 90%, which corresponds to a 0.1 mag.

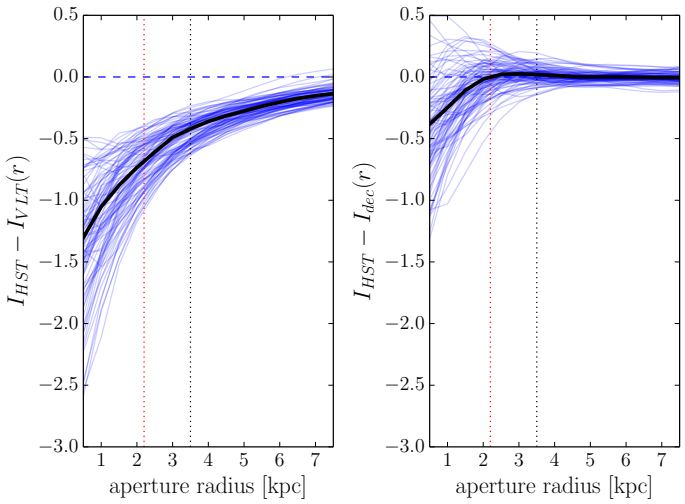

Fig. 3. *Left*: differences between the aperture photometry performed on images obtained with the ACS at the HST and on the original FORS2 images. *Right*: the difference between the aperture photometry performed on the deconvolved FORS2 and the images of the ACS at the HST. Ninety percent of the ACS PSF energy is contained inside a 2.2 kpc radius, shown as the dotted red line. The measurements made on the HST and the VLT-deconvolved images down to 3.5 kpc from the centre of the galaxy (black dotted line) agree excellently well.

Taking the still large scatter between the HST and deconvolved-VLT magnitudes at $r = 0.3''$ into account, we conservatively set the bulge aperture limit to $r = 0.5''$ (the angular sizes apply to our redshift range). This ensures that the contamination of the disc by the bulge light is smaller than 0.05 mag. This remains also true for the V-band images because bulges tend to be smaller in the blue. We wish to compare galaxies at different redshifts, therefore we carried out our measurements on physical instead of on angular scales, that is, $r_{\rm ap,in} = 3.5$ kpc. The corresponding angular apertures (red circles in Fig. 2) were calculated for each galaxy based on its redshift. They were typically between 0.45″ ($z = 0.8$) and 0.6″ ($z = 0.4$). The galaxy sizes extend from 0.5″ to 2.5″ with a mean at 1″. For the smallest galaxies, only 25−30% of their surface was therefore kept to retrieve the photometry of the discs. However, even though the uncertainty became large, the measurement was still possible. Photometric errors were tracked down at all steps of the analysis.

4. Colours of the discs

Figure 4 shows the colour–magnitude diagrams of the spiral galaxies in the ten EDisCS clusters. At this stage, colours and magnitudes are still from the original EDisCS photometry, meaning that they are integrated over the full galaxy before deconvolution. In each panel, we identify the cluster members and field galaxies with redshift $z = z_{\rm cl} \pm 0.03$. This field galaxy selection was chosen to avoid crowding in the diagram. In each panel, we show the position of the red sequence of the clusters calculated as in De Lucia et al. (2007). Field and cluster spirals cover very comparable locii in the CMDs, whereby we exclude strong biases in the comparison of the properties of two populations.

4.1. Comparison between field and cluster population

We now explore the relation between the colours of the discs and the morphological types of their parent galaxies in the field

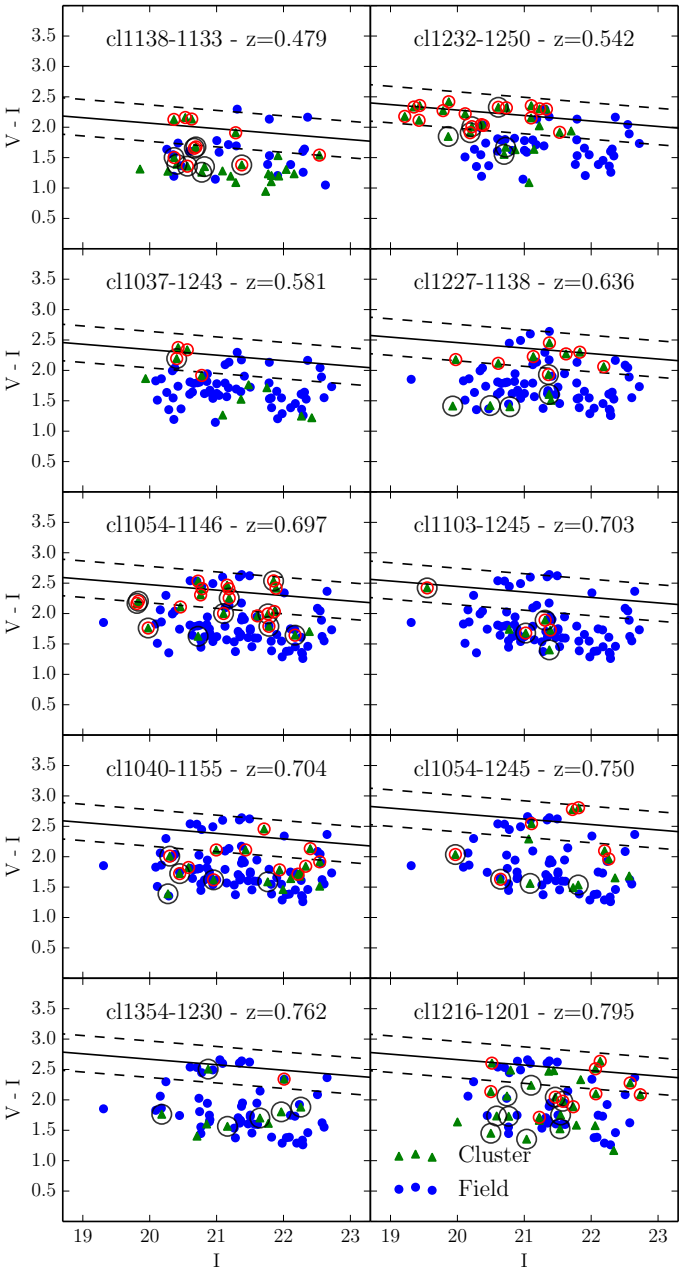

Fig. 4. Colour–magnitude diagrams of the spiral galaxies in the ten EDisCS clusters. In each panel, the green triangles indicate the cluster members. The blue points are the field galaxies within ±0.03 the cluster redshift with or without HST imaging (see Sect. 2). The solid thick lines represent the red sequence best-fit relations, using all the cluster members and a bi-weight estimator (Beers et al. 1990), and assuming a fixed slope of $\alpha = -0.09$ as in De Lucia et al. (2007). The dashed lines correspond to a ±0.3 mag deviation from this best-fit line. The red circles identify galaxies with discs redder than their field counterparts, i.e., at same redshift and with same morphological type, as identified in Fig. 6. The black circles show the galaxies that were detected at 24 μm with *Spitzer*.

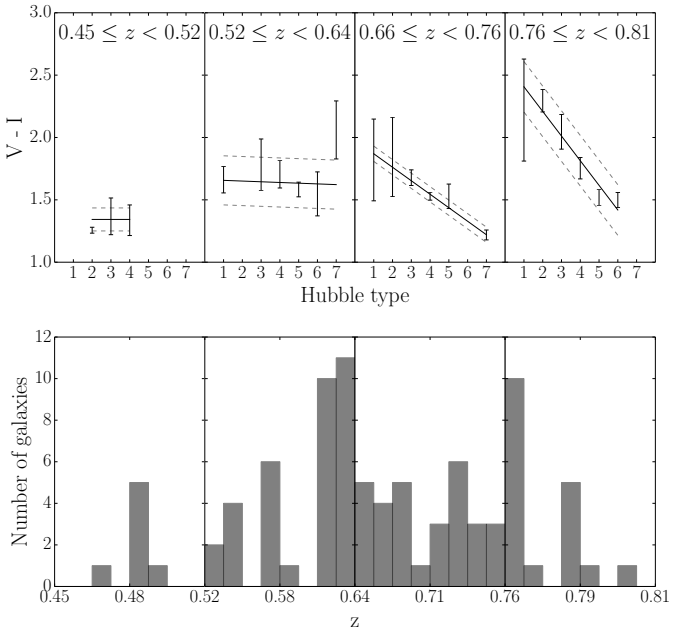

Fig. 5. Colour-morphology relation for the discs of field galaxies at different redshifts. In each of the upper panels the solid lines show the best fit of the relation that is obtained by keeping both the slope and the y-intercept as free parameters. The dashed lines show the 1σ confidence interval, computed from the covariance matrix of the fits. These fits are used to infer the relative colour properties of field and cluster discs. The lower panel shows the redshift distribution of the galaxies inside each redshift bin.

and clusters. This time colours are obtained after and by the deconvolution.

Figure 5 presents the mean colour of the spiral discs in the field and its dispersion as a function of the galaxy Hubble type. The error bars correspond to the dispersion around the mean value at each morphological type. In the rare cases of only one galaxy, we plot its photometric error.

We grouped the galaxies per redshift bin by considering the position of the V and I filters with respect to the 4000 Å break. Although the V and I filters probe gradually bluer parts of the galaxy spectra from the highest to the lowest redshift, $V - I$ nevertheless brackets the 4000 Å break over the full redshift range. The resulting redshift partition yields four groups, $0.45 \leq z < 0.52$, $0.52 \leq z < 0.64$, $0.66 \leq z < 0.76$, and $0.76 \leq z < 0.81$ and 89 field galaxies. The field comparison at $0.45 \leq z < 0.52$ is only used for cl1138.2-1133. In each of the redshift groups, galaxies have masses between $\sim 10^9$ and 10^{11} $M_\odot$ as calculated with iSEDfit (Moustakas et al. 2011).

Discs become clearly bluer towards later morphological types at $z \gtrsim 0.64$ when the V filter gathers a majority of the light at a restframe wavelength shorter than 3500 Å. The slope of the relation between $V - I$ and the galaxy Hubble type becomes steeper with increasing redshift, which is essentially due to the reddening of the discs of the earliest Hubble type galaxies. This is expected from the shift in zero-point of the red sequences (De Lucia et al. 2007), +0.4 mag from $z \sim 0.5$ to $z \sim 0.8$.

The relations between the colours of the discs and the galaxy Hubble types in the field are indicated again in Fig. 6, where we present the distribution in $V - I$ for the discs of spirals in clusters. The three clusters cl1054.4-1146 ($z = 0.6965$, $\sigma_{\rm cl} = 589$ km s^{-1}), cl1040.7-1155 ($z = 0.7020$, $\sigma_{\rm cl} = 418$ km s^{-1}) and cl1103.7-1245b ($z = 0.7029$, $\sigma_{\rm cl} = 242$ km s^{-1}) are grouped together in one single bin at $\langle z \rangle = 0.7$. We provide the number of galaxies per Hubble type at each redshift with histograms.

Figure 6 is used to evaluate whether the colours of spiral discs differ between field and cluster environments. This is done by comparing – at each Hubble type – the $V - I$ disc colours of the cluster galaxies to the colour-morphology relations obtained for the field sample. We can then define three categories: At a given Hubble type, a cluster galaxy disc is defined as blue (red)

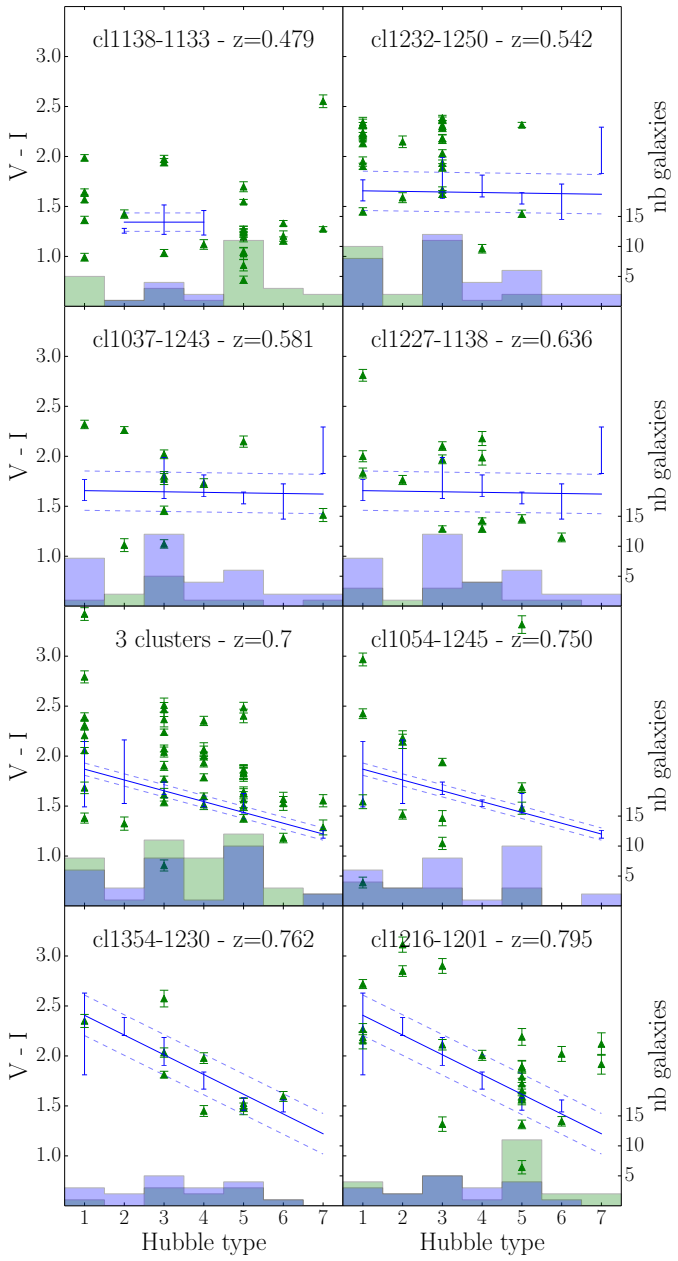

Fig. 6. Colours of the cluster spiral discs, shown with green triangles, as a function of the galaxy Hubble types. The fits of the relations obtained for the field galaxies from Fig. 5 are shown in blue. The histograms show the number of galaxies at each Hubble type for the field (blue) and the clusters (green). The scale is on the right-hand vertical axis.

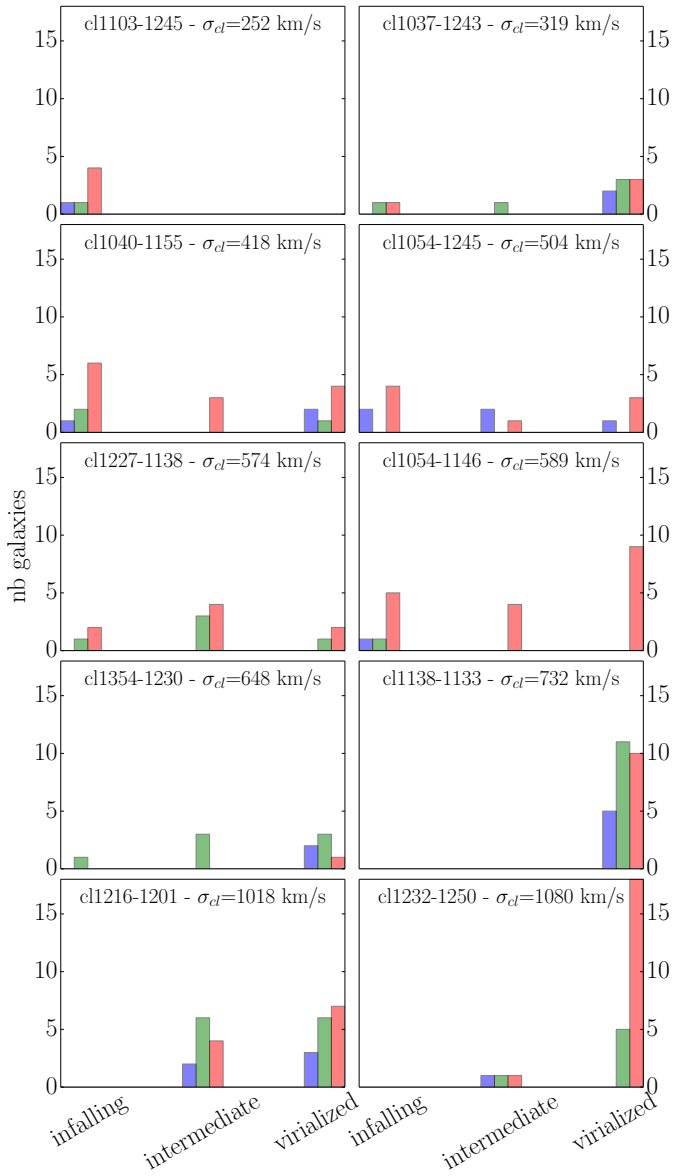

Fig. 7. Distribution of the colour of the spiral discs in clusters. The bar sizes represent the number of galaxies inside each galaxy category: infalling, intermediate, and virialized. Blue stands for cluster discs 1σ bluer than their field counterparts. Red shows the number of cluster discs 1σ redder than their field counterparts, and green illustrates the number of cluster discs with colours compatible with those of their field counterparts.

when its $V - I$ colour, including its uncertainty, is bluer (redder) by more than 1σ (error on the slope on the fit in the field) than the mean value obtained in the field for this morphology. Cluster galaxies with disc colours consistent with their field counterparts (same morphology, same redshift) are called green.

4.2. Spatial distribution

Mahajan et al. (2011) distinguished between virialized, infall, and backsplash classes of galaxies based on their radial velocity and projected clustercentric distances. We applied their scheme to our galaxy sample, using the probability of a galaxy to be virialized, $P_{\rm vir}$ from their Table 2. Virialized galaxies have clustercentric distances smaller than the cluster virial radius, infalling systems prefer large projected distances and high velocities, while the backsplash particles are mostly found just around the virial radius and have low absolute line-of-sight velocities. In the following, we define three categories: galaxies with $P_{\rm vir} > 0.7$ are defined as "virialized", galaxies with $P_{\rm vir} \sim 0.5$ are "intermediate" since they have as much probability to be infalling as to be already virialized. The remaining galaxies are "infalling". Figure 7 summarizes how the colours of discs in cluster compare to discs in the field for each of these three classes. The galaxy counts per cluster are presented as a function of the parent cluster velocity dispersion. Because we compare the disc colours to the mean field population within 1σ, the signature of a cluster disc population compatible with the field would be a normal distribution centred on the green bin (68% of the galaxies). This is not what is observed: Fig. 7 reveals a clear bias of the distribution of

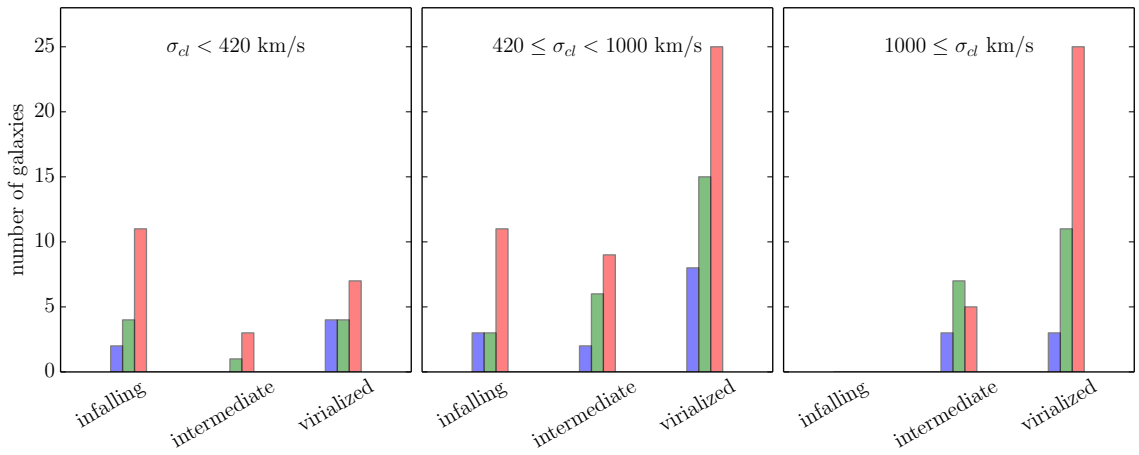

Fig. 8. Same as Fig. 7, but with the clusters binned in velocity dispersion.

Table 2. Fractions of cluster spiral galaxies with discs redder than their field counterparts, N_{red}, as a function of cluster velocity dispersion and redshift.

(a)

σ_{cl} [km s^{-1}]	N_{red}/N_{tot}	$N_{red}/(N_{infall} + N_{inter})$	N_{red}/N_{vir}
$\sigma_{cl} < 420$	0.58	0.67	0.47
$420 \leq \sigma_{cl} < 1000$	0.55	0.59	0.52
$1000 \geq \sigma_{cl}$	0.56	0.33	0.64

(b)

z	N_{red}/N_{tot}	$N_{red}/(N_{infall} + N_{inter})$	N_{red}/N_{vir}
$0.52 \leq z < 0.64$	0.62	0.50	0.68
$0.66 \leq z < 0.76$	0.74	0.71	0.80
$0.76 \leq z < 0.81$	0.32	0.25	0.36

Notes. The parts (a) and (b) of the table correspond to Figs. 8 and 9, respectively. N_{tot} is the total number of galaxies. N_{infall} is the number of infalling galaxies, N_{inter} the number of intermediate galaxies, and N_{vir} the number of virialized galaxies.

the cluster galaxies towards redder discs for the majority of the clusters.

4.3. Cluster mass

To increase the statistical significance of our result, we now bin the clusters in velocity dispersion, σ_{cl}, in Fig. 8. We split the sample into three categories: low ($\sigma_{cl} < 420$ km s^{-1}), moderate ($420 \leq \sigma_{cl} < 730$ km s^{-1}), and high ($\sigma_{cl} > 1000$ km s^{-1}) velocity dispersions. The fractions of red discs are explicitly given in Table 2 for the full sample together with the infall, intermediate, and virialized galaxies. The prominence of galaxies with red discs clearly depends neither on the mass of their parent cluster nor on whether the galaxies are in the infall, intemediate, or virialized group.

We also tested the robustness of our results by removing one cluster at a time in each σ_{cl} bin and checking any change in the global features of Fig. 8. Cl1232.5-1250 ($z = 0.54$) is the only cluster that affects the distribution of its group. Given its size and relatively low redshift, we essentially only sample its virialized region. It is indeed one of the two most massive clusters of our sample, the other one being cl1216.8-1201 ($z = 0.79$) at much higher redshift. The group of the $\sigma_{cl} > 1000$ km s^{-1} clusters obviously suffers from degeneracy between evolution with time and mass.

Without cl1232.5-1250 and cl1216.8-1201, that is, restricting the analysis to structures with σ_{cl} from 252 km s^{-1} to 732 km s^{-1}, we find that ~50% of the spiral galaxies have a disc redder than the mean field population regardless of the cluster mass in which they reside. This is much more than the expected 16% (fraction outside the 1σ probability distribution) we expect to measure if the cluster and field populations were similar.

Cl1232.5-1250 clearly stands out because its fraction of spirals with red discs is larger than the rest of the investigated structures. Similarly, in our hightest redshift bin, the fraction of red discs is higher in cl1216.8-1201 ($\sigma = 1080$ km s^{-1}) than in cl1354.2-1230 ($\sigma = 648$ km s^{-1}). This suggests that that either extremely dense environments act as particularly efficient star formation suppressors or that galaxies in these massive clusters have been perturbed longer.

4.4. Look-back time

Figure 9 groups galaxies in redshift bins. For each cluster galaxy we calculated the difference in colour, $\delta(V - I)$, between its colour and the mean colour of the field galaxies in its redshift bin $\delta(V - I) = [V - I]_{cl} - [V - I]_{field}$. The mean and the dispersion of these colour shifts are indicated, with values given on the right y-axis of the figure. The error bars are the standard deviation around the mean $\delta(V - I)$.

Figure 9 reveals a sharp increase in the number of reddened discs below $z = 0.76$. The lowest and highest z bins are dominated in number by cl1232.5-1250 and cl1216.8-1201, respectively. Nevertheless, cl1216.8-1201 and cl1354.2-1230 in the high-z bin share consistent disc properties in that they encompass a smaller fraction of spirals with red discs than cluster at lower redshift. Similarly, removing cl1232.5-1250 from the low-z bin diminishes the number of red discs in its groups, but they still represent the dominant population. In conclusion, the increase in the number of galaxies with reddened discs below $z = 0.76$ is a robust result of our analysis. Its general significance must be assessed in more detail by conducting similar studies at higher redshift, as our small number of clusters at $z \geq 0.75$ makes us sensitive to possible variance.

4.5. Extinction

The observed colour reddening of the cluster discs might be caused in principle by some highly inclined and therefore

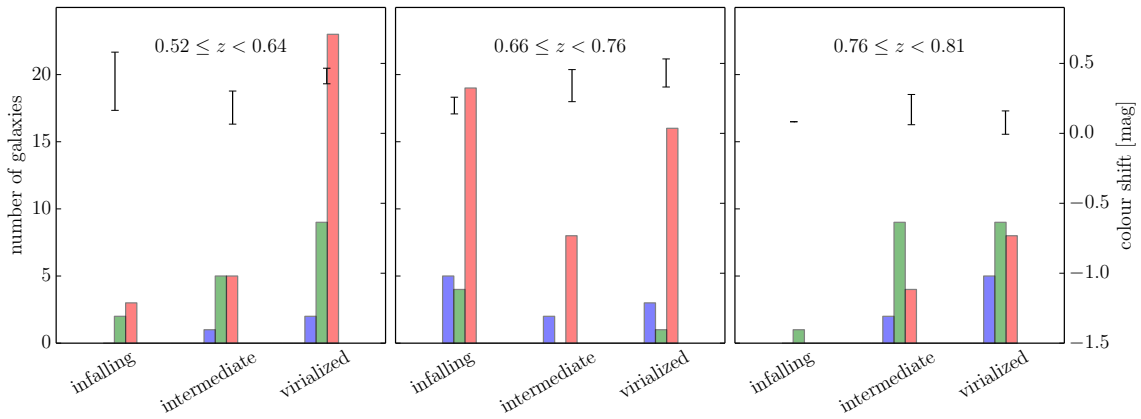

Fig. 9. Same as Figs. 7 and 8, but with the clusters binned in redshift. The mean colour shift, $\delta(V-I)$, between the field disc colours and the cluster disc colours is given for each galaxy type and for each redshift bin. The scale of these shifts is provided on the right-hand vertical axis. The error bars correspond to the dispersion around this mean value.

dust-extinct galaxies. We know from Fig. 1 that our cluster and field global populations follow the same distribution of inclination angles. However, these distributions may vary within each redshift, $\sigma_{\rm cl}$ or virialization bin and thereby cause a shift in $V-I$. To determine this potential bias, we used the inclination angles computed on the images obtained with the ACS at the HST (Simard et al. 2009) to exclude galaxies with angles larger than 70°. This inclination is available for 158 cluster members and 77 field galaxies. Once discarded, the highly inclined galaxies, 63 field galaxies and 114 cluster galaxies remain and our results are unchanged. In conclusion, strongly inclined galaxies do not drive the observed reddening of some of the discs in clusters.

5. Discussion

In all redshift groups, galaxies in clusters clearly deviate from a normal distribution centred on the properties of the field galaxies. In the $0.52 \leq z < 0.64$ and $0.66 \leq z < 0.76$ groups, ~60% and 70% of discs, respectively, are redder than their field counterparts. Above $z = 0.76$, the discs in the field and in clusters appear to have more comparable stellar populations, with a total fraction of red discs of only ~30%. Calculating the binomial probabilities of such events rejects at 99% confidence level that the cluster populations could be built from the field sample.

Figure 4 reveals that this redder disc population is not restricted to the cluster red sequences and can also be found in the cluster blue sequence. This is particularly clear with increasing lookback time. We flag the galaxies in Fig. 4 that were detected by Spitzer at 24 μm (Finn et al. 2010), when those observations were available. At $z = 0.79$, our 80% star formation rate completeness limit is ~14 $M_{\odot}$/yr, while at $z = 0.48$ we reach 5 $M_{\odot}$/yr.

Figure 10 presents the distribution of our sample disc galaxies in the two restframe colour diagram $U-V$ versus $V-J$. The U, V, and J magnitudes are total, meaning they are integrated over the whole galaxies and are derived from our ground-based photometry (White et al. 2005) using the technique of Rudnick et al. (2006) and Rudnick et al. (2009). The colours of the points distinguish between the cluster galaxies i) that are located on the red sequence with discs redder than their field counterparts (in red). These red-on-redseq galaxies (for red disc galaxies on the red sequence) compose ~24% of our full sample. ii) Galaxies that are not located on the red sequence, but with discs redder than their field counterparts (in orange). These red-not-on-redseq galaxies compose another ~24% of our sample of cluster galaxies. Finally, iii) galaxies that are not located on the red sequence with disc colours similar to their field counterparts (in green). Following Williams et al. (2009), we indicate the dividing line between star-forming and passive galaxies. It is striking to see how well the properties of the discs reveal the properties of their parent galaxies.

5.1. Red-sequence galaxies

The vast majority (80%) of the galaxies that lie on the cluster red sequences are also located in the region of the $(U-V, V-J)$ plane where the systems that have stopped forming stars are expected to be. Visual inspection of the images of the remaining galaxies reveal that these 20% are composed of inclined dusty star-forming galaxies. Most of them are detected by *Spitzer*. If our sensitivity at 24 μm had been higher, we would probably have detected them all. The left panel of Fig. 11 provides a typical example of a red spiral galaxy whose star formation has been quenched, shows its HST/*F814W* image, and its FORS2 spectrum. While the spiral arms can still be identified, dust lane and clumps of young stars are absent. The optical spectrum is typical of an old (>5 Gyr) stellar population with strong CN molecular bands below 3900 Å. Interestingly, this type of galaxies is found in all clusters regardless of their mass. Some of them belong to the category of infalling galaxies, but most belong to the virialized groups defined in the previous section. This means that galaxies can be pre-processed before they are trapped in the cluster potential well. Correcting for the galaxies that lie on the red sequence because of their inclination and high dust content, the fraction of genuinely passive spiral galaxies constitutes 20% of our sample. This result combines ten clusters and corresponds to the fractions of Moran et al. (2006), 27%, in the cluster Cl0024+17 at $z = 0.4$ (possibly including galaxies with residual star formation), 17% in (Wolf et al. 2009) in A901/2 at $z = 0.17$. Red passive galaxies are also observed in low-density environments (Poggianti et al. 1999; Goto et al. 2003; Masters et al. 2010), but at lower frequencies.

5.2. Blue-sequence galaxies

The right panel of Fig. 11 shows a typical example of red-not-on-redseq galaxy with red disc, but whose colour and magnitude do not place it on its cluster red sequence. This time, dusty star-forming regions appear clearly, although not on all arms. The

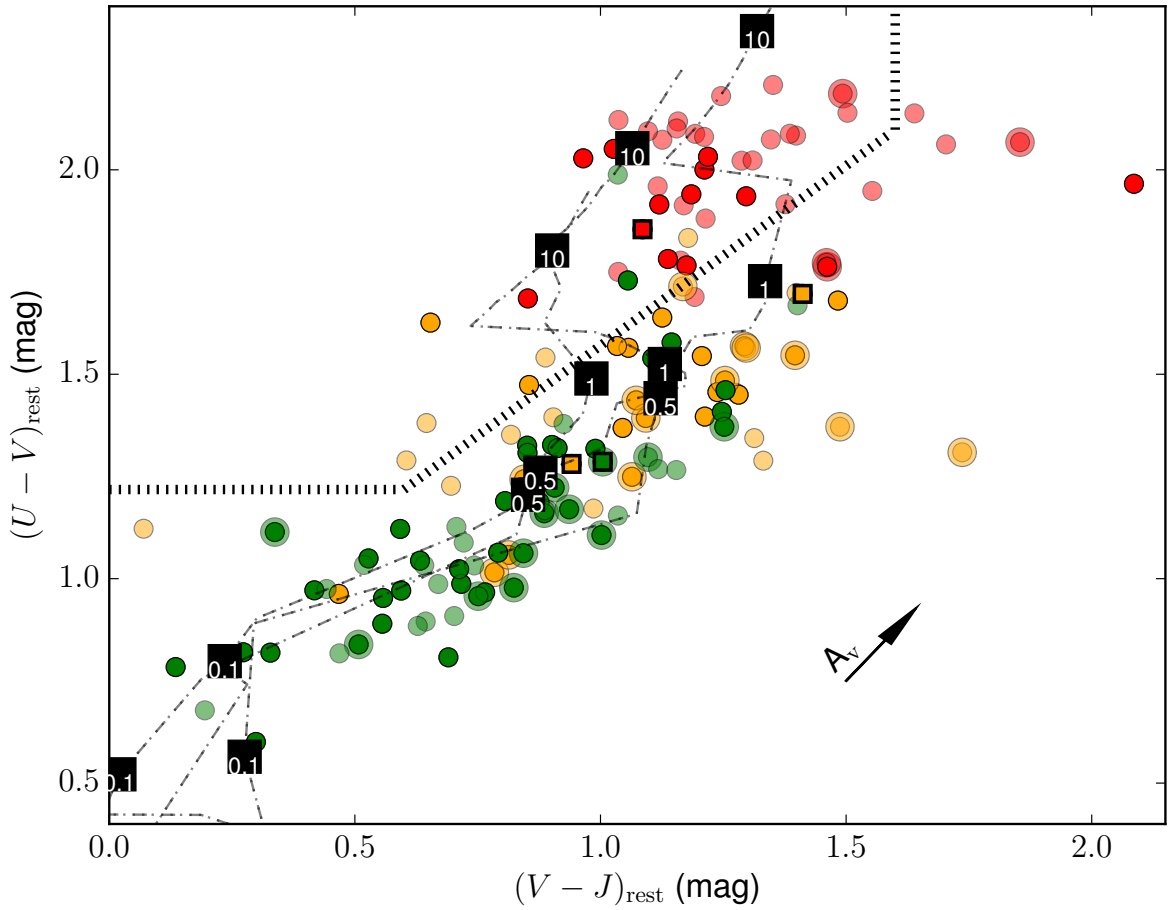

Fig. 10. Rest frame $U - V$ versus $V - J$ diagram. Galaxies with disc colours compatible with their field counterparts are shown in green. Galaxies that are still forming stars, but whose discs are nonetheless redder than their field counterparts, are plotted in orange. Galaxies with red discs that are on the red sequence are shown in red. Large circles identify galaxies that have been detected at 24 μm with Spitzer and have $\log L_{\rm IR} \geq 10.91$ ($SFR \sim 14\ M_\odot$/yr. Plain colours identify face-on galaxies. The three squares correspond to the three galaxies in Fig. 11. The models of Maraston (1998) and Maraston et al. (2003) are shown as dot-dashed lines, and a few ages of the single stellar population are indicated.

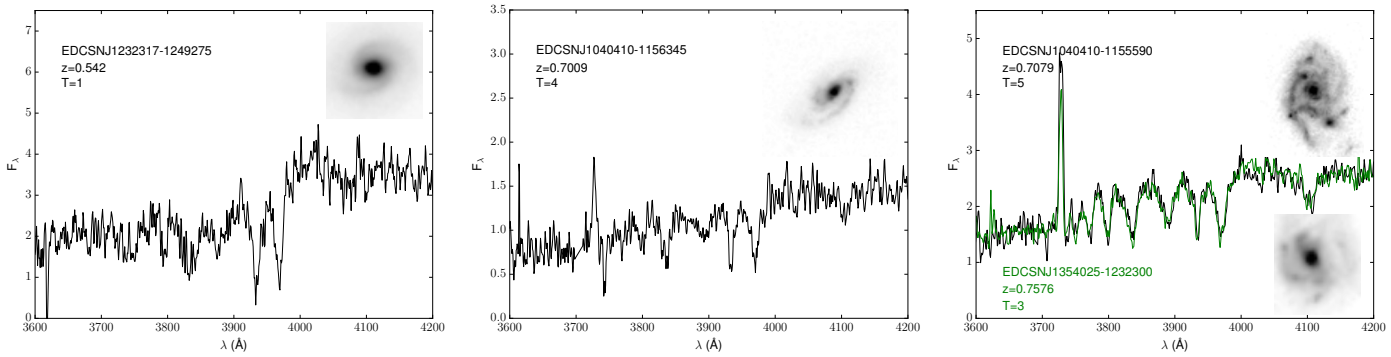

Fig. 11. Three examples of FORS2 spectra. The name of the galaxy, redshift, and T-type are indicated. The *left panel* displays a representative spectrum of a galaxy on the red sequence, whose disc is redder than its field counterparts. The *middle panel* shows the spectrum of a galaxy in the blue sequence, but forming stars at a low rate and with a red disc. The *right panel* displays in black the spectrum of a galaxy that actively forms stars, but with redder disc than its field counterparts. For comparison we show in green a galaxy with a field-like disc that exhibits the same spectral feature and colours as the galaxy in black, but with an earlier morphological T-type.

FORS2 spectrum reveals high-order Balmer lines typical of stellar population younger than 5 Gyr.

We indicate in Fig. 10 the evolutionary tracks of star clusters in the ($U - V$, $V - J$) plane as provided by the models of Maraston (1998) and Maraston et al. (2003). We carefully calibrated the zeropoints of these models against the observations of globular clusters of Frogel et al. (1980) and Bica & Alloin (1986a). We show three metallicities [Z/Z$_\odot$] −0.33, 0., and 0.35, which are representative of the range of mean metallicities of spiral galaxies. Stellar clusters are – to first-order approximation – single stellar populations with fixed age and metallicity, and they are meant to be representative of the mean light-weighted properties of the galaxies. At this stage, we do not need a more detailed population synthesis that takes the full metallicty and age range of the stellar population into account (e.g. Jablonka et al. 1990).

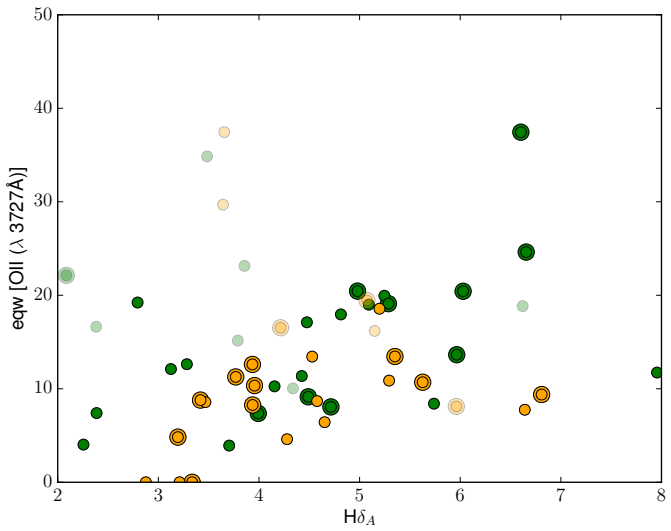

Fig. 12. OII equivalent width versus Hδ_A diagram. Galaxies with disc colours compatible with their field counterparts are shown in green. Galaxies that are still forming stars but whose discs are redder than their field counterparts are plotted in orange.

The key lesson of this exercise is that while extinction runs along the sequence of star-forming galaxies and might naturally be responsible for some of the scatter in their distribution, the aging of the stellar population follows the same direction. This holds until some time between 1 and 5 Gyr, when the stellar population colour–colour evolution becomes perpendicular to the star-forming galaxy sequence, towards bluer $V-J$ and redder $U-V$.

Undoubtely, red-not-on-redseq galaxies are forming stars, hence the question arises whether their discs are redder by dust or because their star formation rates have decreased compared to their field counterparts, which increases the proportion of ageing stars.

To answer this question, we first consider the [OII] λ3727 Å emission line and compare its equivalent width in red-not-on-redseq galaxies and in cluster galaxies that have discs comparable to field ones. The result is shown in Fig. 12, where we show the distribution of the [OII] equivalent width as a function of the Hδ_A equivalent width (Balogh et al. 1999; Worthey & Ottaviani 1997). We show all galaxies, but restrict our analysis to galaxies with low inclination angles (<70 degrees), which are displayed in plain colours, while the others are shown in transparency, to avoid spurious effects to differences in the orientation of the slits with respect to the galaxy major axis. The distribution of the red-not-on-redseq galaxies in the OII-Hδ_A plane is similar to the galaxies compatible with their field counterparts, but lacks the high [OII] equivalent widths at high Hδ_A.

We indicate with large circles galaxies that have been detected by Spitzer at 24 μm, with $\log L_{\rm IR} \geq 10.91$ ($SFR \sim 14\ M_\odot$/yr, the 80% completeness limit of the highest redshift of our cluster, cl1216.8-1201 (Finn et al. 2010). For galaxies with stellar masses above $10^{10}\ M_\odot$ and with a redshift above $z = 0.6$ for which we have sufficient statistics, 59% of the field-like spirals have $SFR \sim 13\ M_\odot$/yr as measured in the far-infrared against 62% for the red-not-on-redseq galaxies. Restricting the sample to the exact same limit in OII equivalent width (7 Å $\leq$ eqw(OII) $\leq$ 15 Å) for the two sets of galaxy populations results in detections of 50% and 57%, respectively. This means that if dust enshrouds star formation, it does it in a similar way in both types of galaxies. Because dust is genuinely associated with star formation, it can add dispersion in the distribution of galaxies along the star-forming galaxy sequence in the $U-V$ vs. $V-J$ plane, but it is not by itself at the origin of the mean location of the red-not-on-redseq and field-compatible galaxies.

There are essentially two degrees of evolution among the red-not-on-redseq galaxies: i) Those that are still actively forming stars, which would hence not be detected in a survey focussing on star formation rate indicators alone as galaxies on the way to be quenched. However, their activity already is or has been for a period diminished with respect to their morphology. A concrete example is provided by EDCSNJ1040410-1155590 (red-not-on-redseq, 0.7079, $\log(M_\star) = 10.94$), whose spectrum is shown in the right panel of Fig. 11. It has the same $U-V$ (∼1.25) and $V-J$ (∼1.) colours as EDCSNJ1354025-1232300 (field-like, $z = 0.7576$, $\log(M_\star) = 11.08$). These galaxies are identified with squares with black borders in Fig. 10. Both galaxies also have very similar OII and Hδ_A equivalent widths, and their spectra are superimposed remarkably well over each other in Fig. 11. EDCSNJ1040410-1155590 was visually classified as T-type=5 (Sc), while EDCSNJ1354025-1232300 has T-type=3 (Sb). EDCSNJ1040410-1155590 is therefore considered red for its Hubble type. ii) The other type of red-not-on-redseq galaxies is an accentuated version of the previous one, in which galaxies have only residual star formation, such as EDCSNJ1040410-1156345 ($U-V \sim 1.4$ and $V-J \sim 1.6$) in the middle panel of Fig. 11. Their spectral signature is a mix between CN absorption and residuals of the high-order Balmer lines, revealing an ageing stellar population. As such, these red-not-on-redseq galaxies are the closest systems to being fully quenched.

Thirty percent of the red-not-on-redseq galaxies are in the infalling group of galaxies, adding evidence that a fraction of galaxies are pre-processed in external structures before reaching the cluster cores.

It is important to stress that while the spatial coverage of each cluster varies simply because a given FORS2 field of view covers larger clustercentric distances of a low-mass cluster than a massive one, the category of the virialized galaxies essentially encompasses only galaxies within $0.5 \times R_{200}$ of all structures, hence allowing a proper comparison between all groups and clusters. This category is the most populated one. Farther out, our statistics is admittedly poorer. Nevertheless, there is a fair indication that a significant fraction of the spirals in small structures ($\sigma_{\rm cl} < 420$ km s^{-1}, 2 groups at $z = 0.70$, one at $z = 0.58$) have been perturbed before they reach the cores of the group.

The red-on-redseq galaxies have preferentially early-type morphologies, while the red-not-on-redseq galaxies have later (T-Type ≥ 5) ones. This is easily understandable since there is a genuine strong correlation between morphologies, colours, and star formation rate (e.g. Fig. 3 in Kennicutt 1998; Jansen et al. 2000). Once their SFR are lower, the earlier types may soon reach the red sequence, while the more strongly star-forming systems still remain on the blue sequence or the green valley of the colour–magnitude diagrams.

5.3. Timescales

The time it takes for a galaxy to stop forming stars is a long-standing question. Figure 6 shows that there is a range in intensity of disc reddening that extends from a minor colour shift $\delta V-I$ to ∼0.5 mag in each redshift bin. This reflects the diversity of galaxy morphologies and associated star formation history to which the variety of infall trajectories onto the cluster central regions must be added.

It is helpful to form an idea of the ages of the stellar populations we consider. The Maraston models plotted in Fig. 10 gives to first approximation light-weighted mean ages of our sample of cluster spirals between 5×10^8 to 1×10^9 yr when galaxies are located on the star-forming system sequence and above 5×10^9 yr otherwise. Since these restframe colours are integrated over the whole galaxies, while colour differences between field and cluster are calculated for the discs alone, we confirmed these estimates by reproducing the $V - I$ colours of the discs alone, as shown in Fig. 6. To do this, we used the observed spectra of globular clusters with metallicities from −1.5 to solar and open clusters with ages spanning 10^8 to 5×10^9 yr, from the database of Bica & Alloin (1986a,b), which we redshifted.

It is interesting to note that 58% of the galaxies in the virialized groups of galaxies are still forming stars. Some at a slower pace than others and already redder than their field counterparts, but all active. Not only do these results robustly confirm that galaxies are able to continue forming stars for some significant period after being accreted into clusters, they also suggest that star formation can decline on seemingly long timescales, as revealed by the existence of red-not-on-redseq galaxies. These galaxies are still forming stars, but for their colour to become redder, some of them must have diminished star formation rates for several Gyr (1 to 5 Gyr) (e.g. Fig. 10). The proportion of younger and older stars must slowly change to favour the latter. Our conclusion agrees with the findings of some recent works that favoured long (1−4 Gyr) quenching timescales (Balogh et al. 2000; Finn et al. 2008; De Lucia et al. 2012; Taranu et al. 2014; Haines et al. 2015).

Koopmann & Kenney (2004) analysed galaxies with reduced total star formation in the Virgo cluster in which they took into account the Hubble type of their galaxies as we do. They found that these systems have truncation (more centrally concentrated Hα extent than normal systems) rather than anemia (low Hα surface brightness across the disk), which causes the reduced total star formation rates. It is too early to conclude on this part for our sample, although Jaffé et al. (2011) found OII truncated at $1-2\sigma$ significance in the EDisCS spirals for a subsample of the present sample. Further investigations both in OII and Hα are planned.

6. Conclusion

We presented the first analysis of the $V - I$ disc colours in cluster and field spiral galaxies at intermediate redshift that is free of any prior on the shape of the galaxy luminosity profiles.

We deconvolved the V and I images of 172 cluster and 96 field spiral galaxies obtained with FORS2 at the VLT with initial resolution of 0.48″ to 0.85″ and achieved a final spatial resolution of 0.1″ with 0.05″ pixels; this is close to the resolution of the ACS at the HST. After removing the central 3.5 kpc of each galaxy to avoid contamination by the bulges, we measured the $V - I$ colours of the discs and compared them to the mean colour of the discs in field spirals. This comparison was conducted per Hubble type and took both the photometric errors and the dispersion of the relations obtained in the field into account. A cluster galaxy disc was considered to be red (blue) when its $V-I$ colour, including its uncertainty, was redder (bluer) by more than 1σ (error on the slope on the fit in the field) than the mean value obtained in the field for this morphology.

- We find a large portion of spiral galaxies in clusters with $V - I$ colours redder than those in the field at the same morphological type. The prominence of galaxies with red discs depends neither on the mass of their parent cluster nor on whether the galaxies are in the infall, intermediate, or already virialized regions.
- In all redshift groups, galaxies in clusters have disc colours that clearly deviate from a normal distribution centred on the properties of the field galaxies. In the $0.52 \leq z < 0.64$ and $0.66 \leq z < 0.76$ groups, ∼60% and 70% of discs, respectively, are redder than their field counterparts. Above $z = 0.76$, the discs in the field and in clusters appear to share more comparable stellar populations, with a total fraction of red discs of only ∼30%. Calculating the binomial probabilities of such events rejects that the cluster populations could be built from the field sample at 99% confidence level. Future studies in clusters at higher redshift are needed to assess the significance of the lower fraction of redder discs at $z > 0.76$ that we find.
- Passive spiral galaxies constitute 20% of our sample. They are located on the cluster red sequences. These systems are not abnormally dusty; they are are made of old stars and are located on the cluster red sequences.
- Another 24% of our cluster galaxy sample is composed of galaxies that are still active and star forming, but have discs redder than their field counterparts. These galaxies are naturally located in the blue sequence of their parent cluster colour–magnitude diagrams.
- The reddest of the discs in clusters must have stopped forming stars more than ∼5 Gyr ago. Some of them are found among infalling galaxies, suggesting that pre-processing is at work long before galaxies reach the cluster cores.
- Our results confirm that galaxies are able to continue forming stars for some significant period of time after being accreted into clusters. They also suggest that star formation can decline on seemingly long timescales. Galaxies that are still forming stars but have discs redder than their field counterparts must have diminished their star formation rates for 1 Gyr to 5 Gyr to have redder colours.

With ongoing and future wide field surveys such as KIDS, DES, and Euclid, multi-band photometry with matched spatial resolution will become of increasing importance. This is done so far with profile fitting of individual bands, for example with GIM2D Simard et al. (2009), GALFIT Peng et al. (2011), or by simultaneously fitting many bands (Megamorph, Häußler et al. 2013). Direct deconvolution of the data followed by aperture photometry offers an interesting alternative to model fitting, as it does not depend on any prior on the shape of the galaxies to be studied. Any complex structure is restored at high spatial resolution, independently of any underlying model. Our deconvolution method is fast enough to be applied in an automated way to large samples of galaxies. The work presented in this paper may therefore be extended to much larger areas with limited or no HST imaging, but where multi-band images are available from the ground.

Acknowledgements. This work was supported by the Swiss National Science Foundation (SNSF). We warmly thank Yara Jaffe for timely and informative discussions.

References

Aguerri, J. A. L., Iglesias-Paramo, J., Vilchez, J. M., & Muñoz-Tuñón, C. 2004, AJ, 127, 1344
Bahé, Y. M., & McCarthy, I. G. 2015, MNRAS, 447, 969
Balogh, M. L., Morris, S. L., Yee, H. K. C., Carlberg, R. G., & Ellingson, E. 1999, ApJ, 527, 54
Balogh, M. L., Navarro, J. F., & Morris, S. L. 2000, ApJ, 540, 113

Bamford, S. P., Milvang-Jensen, B., & Aragón-Salamanca, A. 2007, MNRAS, 378, L6
Beers, T. C., Flynn, K., & Gebhardt, K. 1990, AJ, 100, 32
Bertin, E., & Arnouts, S. 1996, A&AS, 117, 393
Bica, E., & Alloin, D. 1986a, A&A, 162, 21
Bica, E., & Alloin, D. 1986b, A&AS, 66, 171
Blanton, M. R., & Moustakas, J. 2009, ARA&A, 47, 159
Cantale, N., Courbin, F., Tewes, M., Jablonka, P., & Meylan, G. 2016, A&A, 589, A81
Christlein, D., & Zabludoff, A. I. 2004, ApJ, 616, 192
Chung, A., van Gorkom, J. H., Kenney, J. D. P., Crowl, H., & Vollmer, B. 2009, AJ, 138, 1741
de Jong, R. S. 1996, A&A, 313, 45
De Lucia, G., Poggianti, B. M., Aragón-Salamanca, A., et al. 2007, MNRAS, 374, 809
De Lucia, G., Weinmann, S., Poggianti, B. M., Aragón-Salamanca, A., & Zaritsky, D. 2012, MNRAS, 423, 1277
Desai, V., Dalcanton, J. J., Aragón-Salamanca, A., et al. 2007, ApJ, 660, 1151
Ebeling, H., Stephenson, L. N., & Edge, A. C. 2014, ApJ, 781, L40
Finn, R. A., Balogh, M. L., Zaritsky, D., Miller, C. J., & Nichol, R. C. 2008, ApJ, 679, 279
Finn, R. A., Desai, V., Rudnick, G., et al. 2010, ApJ, 720, 87
Frogel, J. A., Persson, S. E., & Cohen, J. G. 1980, ApJ, 240, 785
Fumagalli, M., & Gavazzi, G. 2008, A&A, 490, 571
Gonzalez, A. H., Zaritsky, D., Dalcanton, J. J., & Nelson, A. 2001, ApJS, 137, 117
Goto, T., Okamura, S., Sekiguchi, M., et al. 2003, PASJ, 55, 757
Gray, M. E., Wolf, C., Barden, M., et al. 2009, MNRAS, 393, 1275
Gutiérrez, C. M., Trujillo, I., Aguerri, J. A. L., Graham, A. W., & Caon, N. 2004, ApJ, 602, 664
Haines, C. P., Pereira, M. J., Smith, G. P., et al. 2015, ApJ, 806, 101
Halliday, C., Milvang-Jensen, B., Poirier, S., et al. 2004, A&A, 427, 397
Häußler, B., Bamford, S. P., Vika, M., et al. 2013, MNRAS, 430, 330
Head, J. T. C. G., Lucey, J. R., Hudson, M. J., & Smith, R. J. 2014, MNRAS, 440, 1690
Hudson, M. J., Stevenson, J. B., Smith, R. J., et al. 2010, MNRAS, 409, 405
Jablonka, P., Alloin, D., & Bica, E. 1990, A&A, 235, 22
Jaffé, Y. L., Aragón-Salamanca, A., Kuntschner, H., et al. 2011, MNRAS, 417, 1996
Jansen, R. A., Franx, M., Fabricant, D., & Caldwell, N. 2000, ApJS, 126, 271
Just, D. W., Zaritsky, D., Sand, D. J., Desai, V., & Rudnick, G. 2010, ApJ, 711, 192
Kennicutt, Jr., R. C. 1998, ARA&A, 36, 189
Koopmann, R. A., & Kenney, J. D. P. 2004, ApJ, 613, 851
Koopmann, R. A., Haynes, M. P., & Catinella, B. 2006, AJ, 131, 716
Magain, P., Courbin, F., & Sohy, S. 1998, ApJ, 494, 472
Mahajan, S., Mamon, G. A., & Raychaudhury, S. 2011, MNRAS, 416, 2882
Maltby, D. T., Gray, M. E., Aragón-Salamanca, A., et al. 2012, MNRAS, 419, 669
Maraston, C. 1998, MNRAS, 300, 872
Maraston, C., Greggio, L., Renzini, A., et al. 2003, A&A, 400, 823
Masters, K. L., Mosleh, M., Romer, A. K., et al. 2010, MNRAS, 405, 783
Milvang-Jensen, B., Noll, S., Halliday, C., et al. 2008, A&A, 482, 419
Moran, S. M., Ellis, R. S., Treu, T., et al. 2006, ApJ, 641, L97
Moustakas, J., Zaritsky, D., Brown, M., et al. 2011, ApJ, submitted [arXiv:1112.3300]
Peng, C. Y., Ho, L. C., Impey, C. D., & Rix, H.-W. 2011, Astrophysics Source Code Library [record ascl:1104.010]
Poggianti, B. M., Smail, I., Dressler, A., et al. 1999, ApJ, 518, 576
Poggianti, B. M., von der Linden, A., De Lucia, G., et al. 2006, ApJ, 642, 188
Poggianti, B. M., Desai, V., Finn, R., et al. 2008, ApJ, 684, 888
Rodríguez Del Pino, B., Bamford, S. P., Aragón-Salamanca, A., et al. 2014, MNRAS, 438, 1038
Rudnick, G., Labbé, I., Förster Schreiber, N. M., et al. 2006, ApJ, 650, 624
Rudnick, G., von der Linden, A., Pelló, R., et al. 2009, ApJ, 700, 1559
Simard, L., Willmer, C. N. A., Vogt, N. P., et al. 2002, ApJS, 142, 1
Simard, L., Clowe, D., Desai, V., et al. 2009, A&A, 508, 1141
Taranu, D. S., Hudson, M. J., Balogh, M. L., et al. 2014, MNRAS, 440, 1934
Vika, M., Bamford, S. P., Häußler, B., et al. 2013, MNRAS, 435, 623
Villalobos, Á., De Lucia, G., Borgani, S., & Murante, G. 2012, MNRAS, 424, 2401
White, S. D. M., Clowe, D. I., Simard, L., et al. 2005, A&A, 444, 365
Williams, R. J., Quadri, R. F., Franx, M., van Dokkum, P., & Labbé, I. 2009, ApJ, 691, 1879
Wolf, C., Aragón-Salamanca, A., Balogh, M., et al. 2009, MNRAS, 393, 1302
Woo, J., Dekel, A., Faber, S. M., & Koo, D. C. 2015, MNRAS, 448, 237
Worthey, G., & Ottaviani, D. L. 1997, ApJS, 111, 377